

Article

Target Tracking Algorithm Based on Adaptive Strong Tracking Extended Kalman Filter

Feng Tian ^{1,2} , Xinzhao Guo ^{2,*}  and Weibo Fu ²

¹ Xi'an Key Laboratory of Network Convergence Communication, Xi'an University of Science and Technology, Xi'an 710054, China; tianfeng@xust.edu.cn

² College of Communication and Information Technology, Xi'an University of Science and Technology, Xi'an 710054, China

* Correspondence: guoxinzhao24@163.com

Abstract: Kalman filtering is a common filtering method for millimeter-wave traffic radars. The proposal is for an Adaptive Strong Tracking Extended Kalman Filter (EKF) algorithm that aims to address the issues of classic EKF's low accuracy and lengthy convergence time. This method, which incorporates time-varying fading effects into the covariance matrix of the traditional EKF, is based on the ST algorithm. It allows the recalibration of the covariance matrix and precise filtering and state estimation of the target vehicle. By altering the fading and attenuating factors of the ST algorithm and using orthogonality principles, many fine-tuned fading factors produced from least-squares optimization are introduced together with regionally optimum attenuation factors. The results of Monte Carlo experiments indicate that the average velocity inaccuracy is reduced by at least 38% in comparison to existing counterparts. The results validate the efficacy of this methodology in observing vehicular movements in metropolitan regions, satisfying the prerequisites of millimeter-wave radar technology for traffic monitoring.

Keywords: traffic detection; millimeter-wave radar; radar data processing; strong tracking filter; EKF



Citation: Tian, F.; Guo, X.; Fu, W. Target Tracking Algorithm Based on Adaptive Strong Tracking Extended Kalman Filter. *Electronics* **2024**, *13*, 652. <https://doi.org/10.3390/electronics13030652>

Academic Editor: Hirokazu Kobayashi

Received: 14 January 2024
Revised: 30 January 2024
Accepted: 2 February 2024
Published: 4 February 2024



Copyright: © 2024 by the authors. Licensee MDPI, Basel, Switzerland. This article is an open access article distributed under the terms and conditions of the Creative Commons Attribution (CC BY) license (<https://creativecommons.org/licenses/by/4.0/>).

1. Introduction

Roadway traffic data collecting is a prerequisite for intelligent transportation systems. Based on where they are installed, traffic information-gathering devices are classified as either intrusive or non-invasive [1]. Inside highways, intrusive sensors are used, primarily in the form of magnetic and inductive loop sensors [2]. The majority of non-intrusive sensors, which include millimeter-wave sensors [3,4], laser sensors [5,6], and video image sensors [7–9], are placed on either side or above roadways. In monitoring circumstances, non-intrusive sensors may track the trajectory of vehicle targets using multi-target tracking technology to accomplish tasks including traffic flow statistics, lane coverage, and infraction detection. They are gradually taking the place of intrusive sensors in recent years due to their cheaper installation and maintenance costs. While image processing may extract other details like models, colors, and license plates, it is weather-dependent. Lidar is typically employed in automobiles and offers good comprehensive performance, but it is costly. Millimeter-wave radar provides longer development potential in the field of traffic because of its advantages, which include its all-weather operation, compact size, low cost, and increased detection range [10–14].

The most important tasks in intelligent transportation systems include vehicle tracking estimation, which is categorized under conventional nonlinear filtering problems [15]. Thus, developing a tracking system specifically for urban roadways is quite important [16,17]. Bayesian estimation theory offers a strict framework for nonlinear filtering. In linear Gaussian systems, the Kalman filter (KF) [18] provides the best option for Bayesian estimation in linear Gaussian systems. However, in situations with nonlinear vehicle motion and sensor noise, its efficacy can be limited [19]. The hunt for more accurate tracking and enhanced

flexibility has led to the investigation of more resilient filtering techniques as a main field of study.

Cai [20] developed an optimal Kalman filtering that computes state mean and covariance for traffic flow prediction, which is based on the maximum correlation criterion. TKhalkhali [21] improved tracking performance with the introduction of the interactive adaptive Kalman filter. Ye [22] proposed a novel Adaptive Robust Cubature Kalman Filter (ARCKF) based on the H-infinity volume Kalman Filter (HCKF). Pang [23] introduced an adaptive noise covariance correction mechanism based on normalized innovation squares, which allowed for the precise lateral state estimate of vehicles. Likewise, Chen [24] integrated analytical gain matrices and adaptive factors into the classical desensitized ensemble Kalman filter to estimate the state. Additionally, Ge [25] solved the problem of filter divergence in the Sage–Husa method by providing a direct numerical solution for single noise covariance.

Although combining the KF with other theories has been shown to be effective in monitoring single, constrained motion targets or targets that are limited to particular time periods and locations, it is insufficient for tracking numerous, long-range targets across large distances. The Extended Kalman Filter (EKF) [26] stands out as one of the earliest and most successful applications in nonlinear filtering for tracking vehicle targets, exhibiting significant effectiveness [27–29]. Kaniewski [30] processed this using an Extended Kalman Filter based on an innovative dynamic model derived from a pendulum motion model. Zerdali [31] designed an Adaptive Fading Extended Kalman Filter (AFEKF) observer with improved magnetic flux, velocity, and load torque estimation for control applications that lack velocity sensors.

However, when the vehicle is maneuvering, the observer’s performance considerably declines. To effectively rectify one-step prediction error covariance, Strong Tracking (ST) technology employs a time-varying fading factor that is dependent on the current measurement residue. Significant measurement noise and system interference are present, but the algorithm nevertheless functions effectively and is robust. The anti-interference properties of the ST algorithm and the nonlinear problem-solving capabilities of the EKF are combined in the Strong Tracking Extended Kalman Filter (STEKF). Zhang [32] created an observation technique for unmanned skid-steer vehicles, using EKF theory and noise matrix adaptive estimation to approximate vehicle kinematic parameters. Liu [33] presented the multiple Strong Tracking Cubature Kalman Filter (STCKF) for motion trajectory computation with promising outcomes. Zhang [34] introduced the ASRUKFPU method, an Adaptive Square-Root Untraceable Kalman Filter Phase Untangling technique, which addresses substantial computation mistakes in noisy environments.

Research on the EKF in conjunction with ST theory has produced a number of achievements. Researchers have not acknowledged, nevertheless, the possibility that these new algorithms could alter the core characteristics of the conventional EKF. Ge [35] has experimentally pointed out that it is challenging to consistently determine the superiority of STEKF over EKF in estimating carrier tracking. ST filters, such as EKF, UKF, and CKF, are all basic nonlinear filters that may encounter divergence and error problems caused by subjectively set fading factors. To tackle these issues, Zhang [36] proposed a new fading factor concept and integrated it into the STEKF technique. The method of novel fading factor introduction expands the number of fading factors from one to two by reselecting the introduction positions. Ge [37] redefined the fading factors in the STEKF based on orthogonal principles and developed a new ST Extended Particle Filter (STEPF). Zhang [38] presented an Adaptive Fading Unscented Kalman Filter (AFUKF). Takyi [39] introduced an Adaptive Strong Tracking Extended Kalman Filter (ASTSEKF) that integrates adaptive decay factors, weight adjusters, and ST filters for recursive correction, denoising, and optimization.

This article proposes an Adaptive Strong Tracking Extended Kalman Filter (ASTEKF) for the remote tracking of urban road vehicles using a single millimeter-wave radar. (1) An advantage of the ASTSEKF is the use of orthogonal theory-based adaptive multiple fading elements. By minimizing the effect of state transitions and parameter perturbations on

estimation accuracy, this feature improves adaptability to interferences. (2) The ST method now includes a new adaptive attenuation factor, which is a crucial parameter that is updated every time the fading factor changes. This part helps lessen the divergence problem that strong tracking filtering often encounters. (3) This additional component diminishes the impact of models with a lower degree of match and increases the influence of models that closely match the target state estimations throughout the calculation process. As a result, the algorithm converges more quickly and steadily and shows enhanced capacity to follow abrupt changes in the target's motion states.

2. Materials and Methods

2.1. Target Data Collection

This article makes use of both field data collecting and simulation creation as experimental data. The ZYNQ-7020 baseband signal processing processor under the Xilinx Corporation in San Jose, CA, USA. The CAL60S244 millimeter-wave radar RF chip under the Calterah Corporation in Shanghai, China. along with the MIMO radar system hardware, make up the majority of the data collected for the simulation, which is created using Matlab2021b. The RF board and the baseband board are the two primary components of the radar system. An RF chip, an array transceiver antenna module, etc. are all part of the RF board. Power modules and signal processing modules are among the components of the baseband board. Figure 1 displays the functional block diagram for it.

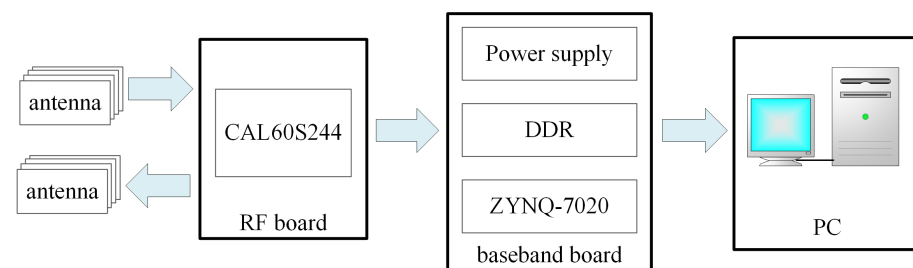


Figure 1. Radar hardware system architecture diagram.

The MIMO radar experimental system operates in the following ways.

Once the parameters have been set, the top computer uses the serial link to send commands to the millimeter-wave radar's RF end, which then processes the commands. To ascertain whether the wave radar's RF end is receiving normally, one needs examine its response data. Simultaneously, the Ethernet port on the host computer is used to receive echo data from the baseband board and to reset the ZYNQ-7020 baseband board.

The central component of the experimental system is the millimeter-wave radar's front end, which functions in accordance with the predetermined mode and system parameters. The linear frequency modulation signal produced by the radar's front end is up-converted to radio frequency (RF) during operation, increased by a power amplifier, and then sent out by the transmit antenna, reflected back when it comes into contact with a target, and picked up by the receive antenna. Following low-noise amplification, down-conversion occurs. ADC is used to obtain the digital signal after sampling the intermediate frequency baseband signal to zero. The millimeter-wave front-end's status signal is fed back to the data acquisition board by the data acquisition board.

Table 1 lists the radar's performance parameters.

The three baseband boards are processed, and the echo data from the millimeter-wave radar's front end are converted into series, parallel, and downshift before being delivered over the network link to the upper computer. A frequency-modulated continuous wave millimeter-wave radar is used to gather data, while at the same time, the camera records video footage of the scene for additional analysis.

Table 1. Millimeter-wave radar parameters.

Performance Index of Radar	Parameter
Operating frequency range (GHz)	60–61
Signal bandwidth (MHz)	200
Distance resolution (m)	0.75
Effective detection distance (m)	20–150
Speed resolution (m/s)	0.5
Angular resolution (°)	1.5

2.2. Modeling the Motion Characteristics of Vehicle Targets

Developing a credible vehicle estimation model is necessary to reliably estimate the motion state. The effectiveness of the filtering method is directly impacted by the complexity of the models, and this in turn influences the accuracy of the results. In order to improve the authenticity of the estimation process, this work employs a simpler mathematical model, namely the Constant Acceleration (CA) model, which is based on the conventional linear two-degree-of-freedom model.

$$\mathbf{X}(k) = [x_k \quad \dot{x}_k \quad \ddot{x}_k \quad y_k \quad \dot{y}_k \quad \ddot{y}_k]^T \tag{1}$$

The model assumes that the target is undergoing uniform acceleration motion on a two-dimensional plane while considering a generalized, nonlinear system model with non-additive noise. It can be represented as follows: $x_k = f(x_{k-1}, w_{k-1})$, $z_k = h(x_k, v_k)$, where x_k represents the target’s state vector at time k , and z_k represents the measurement vector at time k . Both w_k and v_k refer to sequences of process noise and measurement noise, respectively. It is assumed that both w_k and v_k are zero-mean Gaussian white noise with variances of \mathbf{Q}_k and \mathbf{R}_k , respectively.

$$\mathbf{A}(X) = \begin{bmatrix} 1 & T & T^2/2 \\ 0 & 1 & T \\ 0 & 0 & 1 \end{bmatrix} \tag{2}$$

$$\mathbf{B}(X) = \begin{bmatrix} T^2/2 \\ T \\ 1 \end{bmatrix} \tag{3}$$

$$\mathbf{F}(k) = \begin{bmatrix} \mathbf{A} & 0 \\ 0 & \mathbf{A} \end{bmatrix} \tag{4}$$

$$\mathbf{\Gamma}(k) = \begin{bmatrix} \mathbf{B} & 0 \\ 0 & \mathbf{B} \end{bmatrix} \tag{5}$$

The target state vector $\mathbf{X}(k)$ corresponds to the position, velocity, and acceleration in both the x and y dimensions. $\mathbf{F}(k)$ represents the state transition matrix, and $\mathbf{\Gamma}(k)$ represents the process noise covariance matrix.

$$\mathbf{X}(k + 1) = \mathbf{F}(k)\mathbf{X}(k) + \mathbf{\Gamma}(k)\mathbf{v}(k) \tag{6}$$

In the equation, $\mathbf{v}(k) = [v_x, v_y]^T$ represents the noise vector.

The measurement equation represents an assumption about the radar detection process and can be expressed as follows:

$$\mathbf{Z}(k + 1) = \mathbf{H}(k + 1)\mathbf{X}(k + 1) + \mathbf{W}(k + 1) \tag{7}$$

Here, $\mathbf{Z}(k + 1)$ denotes the measurement vector, $\mathbf{H}(k + 1)$ signifies the measurement matrix, $\mathbf{X}(k + 1)$ represents the state matrix, and $\mathbf{W}(k + 1)$ accounts for observation noise.

$$\mathbf{H}(k+1) = \begin{bmatrix} 1 & 0 & 0 & 0 & 0 & 0 \\ 0 & 0 & 0 & 1 & 0 & 0 \end{bmatrix} \quad (8)$$

2.3. Implementation of the Classical Extended Kalman Filter Algorithm

By using the estimate process from the Kalman Filter method to identify the unknown quantities, the EKF seeks to transform the filtering problem of a nonlinear system into a linear one. The computation uses Taylor’s formula to expand the nonlinear function, takes a first-order truncated linearized expansion, and executes KF ignoring higher-order terms beyond the second order. The following formula is used to calculate the EKF algorithm for the nonlinear discrete system:

The \mathbf{F}_{k-1}^x and \mathbf{F}_{k-1}^w Jacobian matrices correspond to the matrix for distance and velocity dimensions, respectively, in the system equations.

$$\begin{aligned} \mathbf{F}_{k-1}^x &= \left. \frac{\partial f(x_{k-1}, w_{k-1})}{\partial x_{k-1}} \right|_{x_{k-1}=\hat{x}_{k-1|k-1}, w_{k-1}=0} \\ \mathbf{F}_{k-1}^w &= \left. \frac{\partial f(x_{k-1}, w_{k-1})}{\partial w_{k-1}} \right|_{x_{k-1}=\hat{x}_{k-1|k-1}, w_{k-1}=0} \end{aligned} \quad (9)$$

The one-step state prediction is represented by $\hat{x}_{k|k-1}$, while the prediction error’s covariance matrix is denoted as follows:

$$\begin{aligned} \hat{x}_{k|k-1} &= f_{k-1}(\hat{x}_{k-1|k-1}, 0) \\ \mathbf{P}_{k|k-1} &= \mathbf{F}_{k-1}^x \mathbf{P}_{k-1|k-1} (\mathbf{F}_{k-1}^x)^T + \mathbf{F}_{k-1}^w \mathbf{Q}_{k-1} (\mathbf{F}_{k-1}^w)^T \end{aligned} \quad (10)$$

$$x_k = f_{k-1}(x_{k-1}, w_{k-1}) \approx f_{k-1}(\hat{x}_{k-1|k-1}, 0) + \mathbf{F}_{k-1}^x \tilde{x}_{k-1|k-1} + \mathbf{F}_{k-1}^w w_{k-1} \quad (11)$$

The \mathbf{H}_k^x and \mathbf{H}_k^v Jacobian matrices correspond to the matrix for distance and velocity dimensions, respectively, in the measurement equations.

$$\begin{aligned} \mathbf{H}_k^x &= \left. \frac{\partial h(x_k, v_k)}{\partial x_k} \right|_{x_k=\hat{x}_{k|k-1}, v_k=0} \\ \mathbf{H}_k^v &= \left. \frac{\partial h(x_k, v_k)}{\partial v_k} \right|_{x_k=\hat{x}_{k|k-1}, v_k=0} \end{aligned} \quad (12)$$

The one-step measurement prediction is represented by $\hat{z}_{k|k-1}$, while the covariance of the innovation, \mathbf{S}_k , and the cross-covariance, \mathbf{C}_k , are denoted as follows:

$$\hat{z}_{k|k-1} = E[z_k | z_{k-1}] = h_x(\hat{x}_{k|k-1}, 0) \quad (13)$$

$$\mathbf{S}_k = \text{cov}(\tilde{z}_{k|k-1}) = \mathbf{H}_k^x \mathbf{P}_{k|k-1} (\mathbf{H}_k^x)^T + \mathbf{H}_k^v \mathbf{R}_k (\mathbf{H}_k^v)^T \quad (14)$$

$$\mathbf{C}_k = \text{cov}(\tilde{x}_{k|k-1}, \tilde{z}_{k|k-1}) = \mathbf{P}_{k|k-1} (\mathbf{H}_k^v)^T \quad (15)$$

The measurement prediction error is given by:

$$z_k = h(x_k, v_k) \approx h_k(\hat{x}_{k|k-1}, 0) + \mathbf{H}_k^x \tilde{x}_{k|k-1} + \mathbf{H}_k^v v_{k-1} \quad (16)$$

$$\tilde{z}_{k|k-1} = z_k - \hat{z}_{k|k-1} \approx \mathbf{H}_k^x \tilde{x}_{k|k-1} + \mathbf{H}_k^v v_k \quad (17)$$

The Kalman gain is determined as:

$$\mathbf{K}_k = \mathbf{C}_k \mathbf{S}_k^{-1} = \mathbf{P}_{k|k-1} (\mathbf{H}_k^v)^T (\mathbf{H}_k^x \mathbf{P}_{k|k-1} (\mathbf{H}_k^x)^T + \mathbf{H}_k^v \mathbf{R}_k (\mathbf{H}_k^v)^T)^{-1} \quad (18)$$

The state update is performed as follows:

$$\begin{aligned} \hat{x}_{k|k} &= E[x_k | z_k] = \hat{x}_{k|k-1} + \mathbf{K}_z (z_k - \hat{z}_{k|k-1}) \\ \mathbf{P}_{k|k} &= \text{cov}(\tilde{x}_{k|k}) = \mathbf{P}_{k|k-1} - \mathbf{K}_k \mathbf{S}_k (\mathbf{K}_k)^T \end{aligned} \tag{19}$$

where the estimation error is $\tilde{x}_{k|k} = x_k - \hat{x}_{k|k}$.

2.4. Improvement Based on the Strong Tracking Extended Kalman Filter Algorithm

Some academics have suggested the Extended Kalman Filter method with inferior fading factors in response to the traditional Kalman filtering algorithm’s low accuracy in calculating state variables [40]. The technique incorporates an adjusted fading factor to address the issue of the asymptotic factor’s propensity to induce over-regulation. When compared to an ordinary filter, the strong tracking filter stands out for its strong robustness even in the case of mismatched model parameters, low sensitivity to noise and initial values, strong tracking ability in the event of an abrupt system state, and moderate computational complexity. The following is how this STEKF-based algorithm has been improved:

Here, the attenuation factor $\beta \geq 1$ is represented. A locally optimal attenuation factor is obtained by using a least squares fit between the cumulative root mean square error $\hat{x}_{k|k}$ and the attenuation factor sequence b_k . The learning step size is denoted by the parameter u , and b_0 is a constant determined empirically.

$$\begin{aligned} bk &= 1 + u \cdot (k - 1), 0 \leq k \\ f(x) &= l1x^5 + l2x^4 + l3x^3 + l4x^2 + l5x + c \end{aligned} \tag{20}$$

$$\beta k = \begin{cases} b_0 & 0 < k \leq 10 \\ bk - 10 | \min(\text{abs}(f(xn))), n = 0, 1, 2 \dots & 11 \leq k \end{cases} \tag{21}$$

The residual covariance matrix is given as:

$$\mathbf{V}_k = \begin{cases} \varepsilon_1 \varepsilon_1^T & k = 1 \\ \frac{\rho \mathbf{V}_{k+1} + \varepsilon_k \varepsilon_k^T}{1 + \rho} & k \geq 2 \end{cases} \tag{22}$$

where ε_k represents the remaining sequence, and $\varepsilon_k = z_k - \hat{z}_{k|k-1}$, $0 < \rho \leq 1$ functions as the forgetting factor conventionally set as $\rho = 0.95$.

To comply with the principle of the residual sequence’s orthogonality, we define the subsequent formula:

$$\left. \begin{aligned} E[(x_k - \hat{x}_k)(x_k - \hat{x}_k)^T] &= \min \\ E(\varepsilon_{k+n} \varepsilon_k^T) &= 0, k = 1, 2, \dots, n = 1, 2, \dots \end{aligned} \right\} \tag{23}$$

$$\left. \begin{aligned} \mathbf{N}_k &= \mathbf{V}_k - \beta \mathbf{R}_k - \mathbf{H}_k \mathbf{Q} \mathbf{H}_k^T \\ \mathbf{M}_k &= \mathbf{H}_k \mathbf{F}_k \mathbf{P}_{k/k-1} \mathbf{F}_k^T \mathbf{H}_k^T \end{aligned} \right\} \tag{24}$$

Taking the trace of Equation (24), one can obtain a suboptimal solution for the attenuation factor λ_k :

$$\lambda_k = \begin{cases} \lambda_0 & \lambda_0 \geq 1 \\ 1 & \lambda_0 < 1 \end{cases}, \lambda_0 = \frac{\text{tr}[\mathbf{N}_k]}{\text{tr}[\mathbf{M}_k]} \tag{25}$$

Substituting Equation (10) results in the prediction error covariance matrix:

$$\mathbf{P}_{k|k-1} = \lambda_k \mathbf{F}_{k-1}^x \mathbf{P}_{k-1|k-1} (\mathbf{F}_{k-1}^x)^T + \mathbf{F}_{k-1}^w \mathbf{Q}_{k-1} (\mathbf{F}_{k-1}^w)^T \tag{26}$$

Compute the multiple suboptimal fading factors, wherein $\alpha_i > 1$ is a constant determined by prior information and $\text{diag}[\mathbf{M}_k]_i$ represents the i -th element on the main diagonal of the matrix \mathbf{M}_k .

$$\lambda_k^i = \begin{cases} \lambda_k = \text{diag}[\lambda_k^1, \lambda_k^2, \lambda_k^3, \dots, \lambda_k^n] \\ \alpha_i c_k, \alpha_i c_k > 1 \\ 1, \alpha_i c_k \leq 1 \end{cases}, c_k = \frac{\text{tr}[\mathbf{N}_k]}{\sum_{i=1}^n \alpha_i \cdot \text{diag}[\mathbf{M}_k]_i} \quad (27)$$

Substituting Equation (26) results in the prediction error covariance matrix:

$$\mathbf{P}_{k|k-1} = \lambda_k \mathbf{F}_{k-1}^x \mathbf{P}_{k-1|k-1} (\mathbf{F}_{k-1}^x)^T + \mathbf{F}_{k-1}^w \mathbf{Q}_{k-1} (\mathbf{F}_{k-1}^w)^T \quad (28)$$

The flowchart of the improved algorithm is shown in Figure 2. Firstly, the vehicle point traces are processed; then, the fading factor, the attenuation factor, and the filtering is calculated. Then, different calculations are performed according to whether the fading factor is greater than 1, the covariance estimate of the filter is updated, and the gain is calculated afterward. Finally, the results of this calculation are used for the next state update, and the results of this filtering are output.

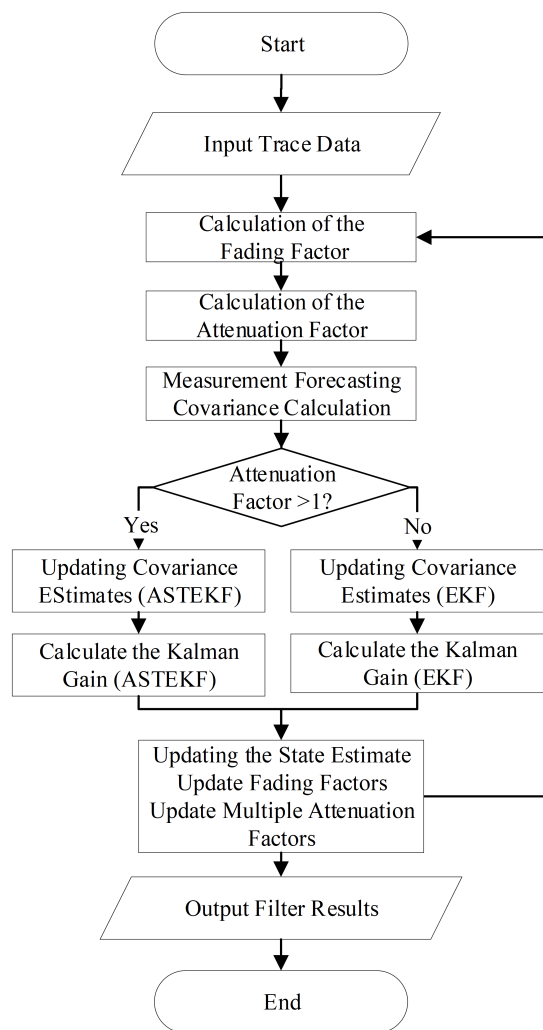


Figure 2. Flowchart of the Adaptive Strong Tracking Extended Kalman Algorithm.

2.5. Simulation Experiments and Analysis

In the simulation experiments in a 2D Cartesian coordinate plane, a Monte Carlo simulation is performed 200 times to ensure the effectiveness of the simulation. Two different target motion states are set to validate the algorithm. The radar is positioned at the coordinate origin $P_r = [X_r, Y_r] = [0, 0]$. The radar has a sampling period of 0.05 s and the total tracking time is 12.5 s. r and θ represent the radial distance and azimuth angle of the

vehicle from the radar, respectively. \mathbf{R}_k denotes the measurement noise, which follows a Gaussian distribution with a fixed standard deviation and a mean of 0. $\mathbf{R}_k(0, [\sigma_r, \sigma_\theta])$. The noise covariance matrix is represented by $\mathbf{R} = \text{diag}[\sigma_r^2, \sigma_\theta^2]$, $\sigma_r = 0.75$ m and $\sigma_\theta = 0.5^\circ$. The negative direction is defined as away from the radar.

The initial state of the target is denoted as $\mathbf{X}_0 = [-8 \quad 0.4 \quad -0.05 \quad 180 \quad -7.5 \quad -0.5]^\top$, and the initial state covariance is $\mathbf{P}_{0|0} = \text{diag}[1 \quad 0.1 \quad 0.01 \quad 1 \quad 0.1 \quad 0.01]^\top$.

$$\mathbf{Z}(k) = \begin{bmatrix} r \\ \theta \end{bmatrix} + \mathbf{R}_k = \begin{bmatrix} \sqrt{x_k^2 + y_k^2} \\ \arctan\left(\frac{y_k}{x_k}\right) \end{bmatrix} + \mathbf{R}_k \quad (29)$$

Target motion 1: The target is initially located at $(-8, 180)$. It undergoes a uniform acceleration motion in the x-axis direction with an initial position of -8 m, an initial velocity of 0.4 m/s, and an initial acceleration of -0.05 m/s². In the y-axis direction, it undergoes a uniform acceleration motion with an initial position of 180 m, an initial velocity of -7.5 m/s, and an initial acceleration of -0.5 m/s².

Target motion 2: The target moves in the same manner as in target motion 1 for the first 2.5 s. After that, there are four velocity changes by the target, occurring every 2.5 s.

Figure 3 shows the trajectory plot for target tracking with filtering. The plot shows the tracking curves of three different types of filters: the black dashed line for EKF tracking, the red line for STEKF tracking, and the blue line for ASTEKF tracking. The true trajectory is represented by the pink dashed line, and the simulated measurement points are represented by the cyan star-shaped markers. Figure 3a shows that the filtering trajectories of the ASTEKF, STEKF, and EKF algorithms closely resemble the genuine trajectory during motion 1. Even when measurements deviate from the norm, the three filtering algorithms track the objective steadily. The target's trajectory shows very little fluctuation, staying mostly unchanged. Specifically, when actual measurements deviate from correct values, STEKF reveals a more substantial disturbance in the following ranges: x-axis -11 to -13 m and y-axis 70 to 40 m. Moreover, in the later portion of the motion, STEKF is most impacted by a higher level of noise interference, which is followed by ASTEKF. EKF performs the best in terms of trajectory tracking stability, which is followed by ASTEKF and STEKF.

The trajectory of motion 2 is shown in Figure 3b as the target segments its uniform acceleration motion in the x and y dimensions. STEKF exhibits the best tracking performance while EKF exhibits the lowest when the target's lateral velocity changes. STEKF shows fast convergence and closely tracks the real values throughout the move from the x-axis at -6.78 to -6.86 m and the y-axis at 140 to 132 m. However, measurement errors later cause significant divergence. The actual measurement values also differ from the expected values when going from the x-axis at -7.75 to -7.9 m and the y-axis at 85 to 75 m, which causes a significant disturbance in STEKF.

Figure 4 shows the Root Mean Square Error (RMSE) of motion 1's position tracking through filtering. When it comes to the vehicle position and position forecasts for the three models, the figure's RMSE of the vehicle's location and velocity shows notable deviations from the original real values. Although STEKF converges the fastest, it is very susceptible to noise and variations in the target's motion state. In contrast, EKF has the slowest convergence and lowest performance. Filtering divergence occurs when alterations in lateral velocity take place along the x-axis. The ASTEKF approach prevents filtering divergence and converges quickly with little error. The target moves uniformly in the x-axis direction—initially in the direction of the radar and then in the opposite direction. The target accelerates uniformly in the y-axis direction toward the radar without changing its motion direction. All three of the filtering methods are able to effectively filter the target in the y-axis direction during the latter stages of motion. Nevertheless, the STEKF algorithm exhibits divergence and subpar tracking throughout the advanced x-axis motion stages. It is clear that integrating ASTEKF with EKF results in relatively small errors in target velocity after stabilization as well as in target location at the start and during the stabilized phase.

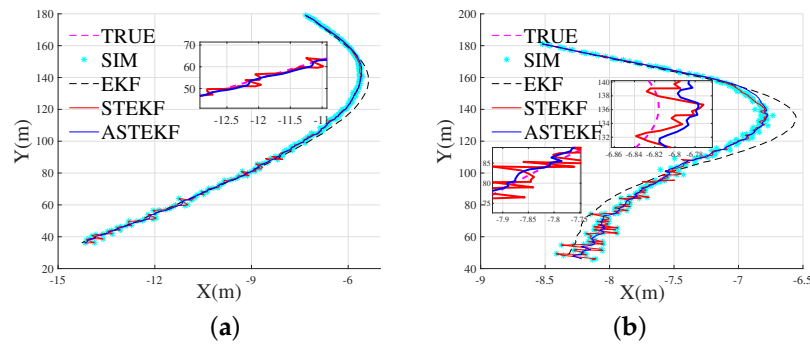


Figure 3. Tracking results for the three filtering algorithms. (a) Tracking diagram for motion 1 filtering. (b) Tracking diagram for motion 2 filtering.

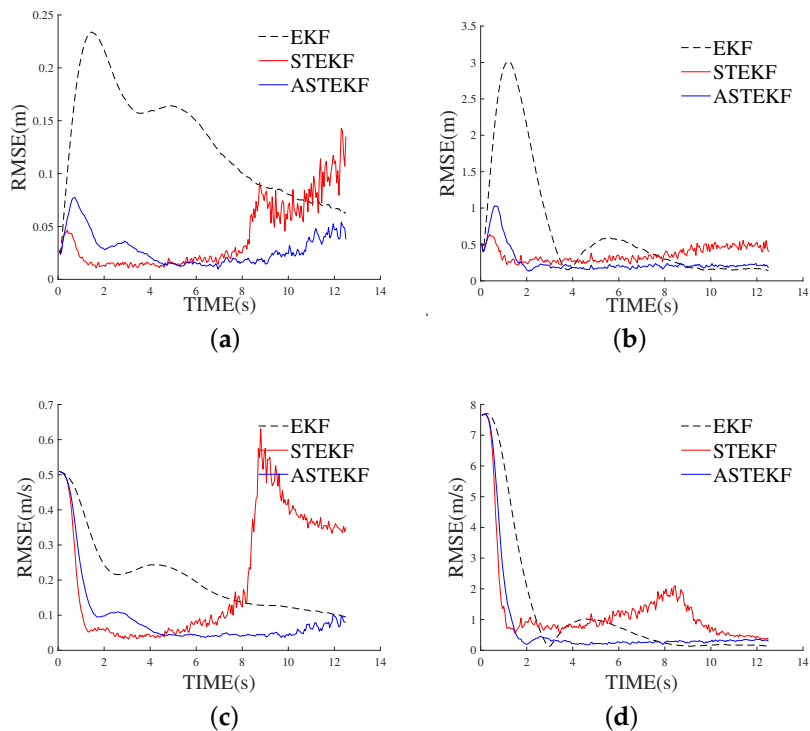


Figure 4. Motion1 filter tracking error plot. (a) RMSE of x-axis position. (b) RMSE of y-axis position. (c) RMSE of x-axis velocity. (d) RMSE of y-axis velocity.

The RMSE for filtering-based motion 2 position tracking is displayed in Figure 5. When moving toward the radar, the object initially moves in the same direction along the x-axis. This is followed by a consistent negative acceleration after 2.5 s when the target’s velocity drops and its acceleration rises. The motion direction shifts away from the radar during this phase. It eventually decelerated uniformly and without direction change after 7.5 s of motion away from the radar. Target acceleration motion along the y-axis is uniform with no change in direction of motion toward the radar. The target advances uniformly toward the radar after 5 s as its acceleration and velocity decrease. Ten seconds later, the acceleration and velocity both pick up, causing the motion to accelerate uniformly in the direction of the radar.

The EKF has delayed convergence, poor tracking of the x-axis location, and ineffective handling of the target’s feeble maneuvering. However, STEKF is unsuccessful for tracking because it converges quickly, achieves minimal error, and is unable to track targets whose motion directions change. ASTEKF exhibits a stable method as it rapidly converges with minimal error.

When tracking velocity along the x-axis, ASTEKF converges quickly and consistently with low error. On the other hand, ASTEKF encounters an initial high error that quickly converges, ultimately attaining good performance, while EKF fails to reach convergence during y-axis position tracking. The target velocity is efficiently filtered in the y-axis direction by all three filtering algorithms. In y-axis velocity tracking, both the ASTEKF and EKF algorithms show favorable convergence; however, STEKF diverges later and is less accurate than EKF.

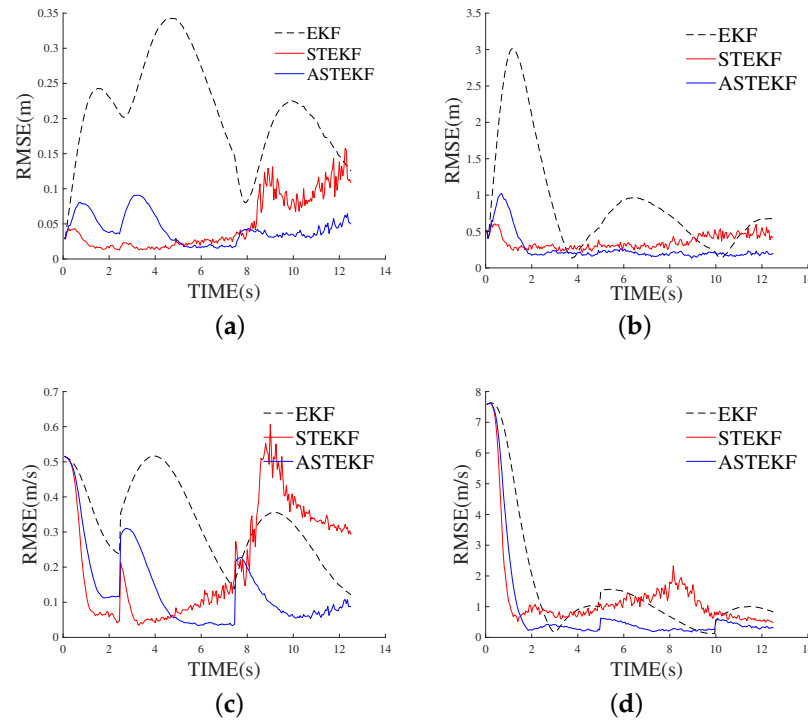


Figure 5. Motion 2 filter tracking error plot. (a) RMSE of x-axis position. (b) RMSE of y-axis position. (c) RMSE of x-axis velocity. (d) RMSE of y-axis velocity.

In combination, the ASTEKF and EKF algorithms effectively and stably filter and track the target’s position and velocity, exhibiting resistance to interference and reliable convergence. Tables 2 and 3 present the average errors for both motion states.

Table 2. Motion 1 mean error table.

Algorithms	X-Axis (m)	Y-Axis (m)	X-Axis (m/s)	Y-Axis (m/s)
EKF	0.1294	0.7022	0.2042	1.2914
STEKF	0.0398	0.3620	0.2073	1.2972
ASTEKF	0.0301	0.2561	0.0924	0.7783

Table 3. Motion 2 mean error table.

Algorithms	X-Axis (m)	Y-Axis (m)	X-Axis (m/s)	Y-Axis (m/s)
EKF	0.2118	0.8949	0.3301	1.6137
STEKF	0.0491	0.3574	0.2185	1.3128
ASTEKF	0.0425	0.2628	0.1375	0.8474

It is evident from the provided tables that the mean errors in position and velocity using ASTEKF filtering are smaller than those using EKF and STEKF filtering. This technique, when compared to EKF and STEKF, reduces the average velocity inaccuracy by about 46% and 38%, respectively, according to calculations. Jitter is present in traditional

STEKF motion trajectories, whereas ASTEKF does not have any jitter, resulting in motion trajectories that are smoother. The ASTEKF filter can successfully monitor a vehicle target whether it is moving normally or changes its speed or direction. This shows that the enhanced ASTEKF is effective in tracking and removing unwanted vehicle targets.

3. Results and Discussion

The experimental setting is located on a three-lane, one-way road in Xi'an, China, as depicted in Figure 6.



Figure 6. Experimental scene and radar in footbridge.

It is challenging to modify fixed window sizes to accommodate the collection of various car kinds in intricate traffic situations. Thus, the primary area of study at this time is the introduction of clustering algorithm-based preprocessing techniques [41]. Due to the limited quantity of data in a single frame, the DBSCAN-based preprocessing approach finds it challenging to reliably aggregate vehicle target locations under false interference. This leads to phenomena like track interruption and track splitting in multi-target tracking. The efficacy of clustering can be enhanced by increasing the density of vehicle target locations using a short-term multiframe data collection technique [42]. Using weighted distance measurements that are gathered quickly (20 frame/s), Figure 7 applies the density-based adaptive noise applied spatial clustering (DBSCAN) algorithm to combine many target trajectories on the main route. Accurately aggregating vehicle track data is possible using this strategy.

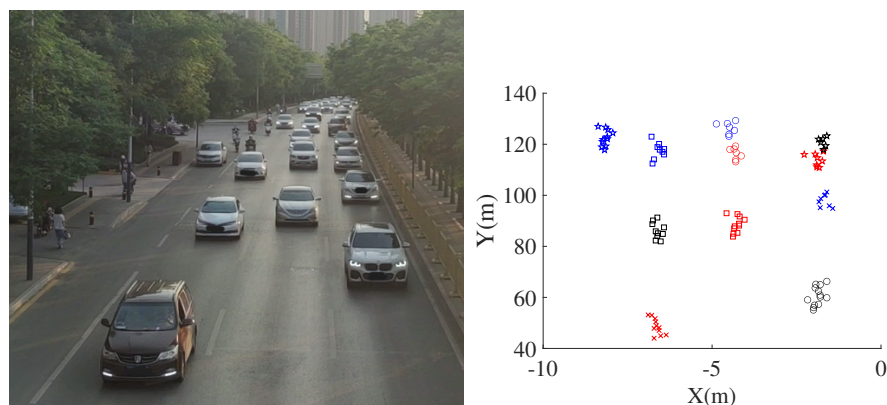


Figure 7. Result of DBSACN algorithm clustering.

As shown in Figure 8, one of the data association methods, Joint Probability Data Interconnection (JPDA) [43,44], aims to relate to the scenario in which observation data, which may originate from several targets, falls into the intersection region of the tracking gate. Calculating the correlation probability between observation data and each target is the goal of JPDA. It makes the assumption that all effective echoes may come from a certain target, but their odds of doing so differ. Using a given number of data, this approach ranks all valid statistical distances and chooses the point with the shortest statistical distance. To build a stable and continuous tracking trajectory for the target, an elliptical wave gate is utilized as a correlation wave gate. The association between the target point trajectory and the trajectory is established based on the maximum correlation probability and the shortest statistical distance. A frequency-modulated continuous wave millimeter-wave radar is used to gather data, while at the same time, the camera records video footage of the scene for additional analysis.

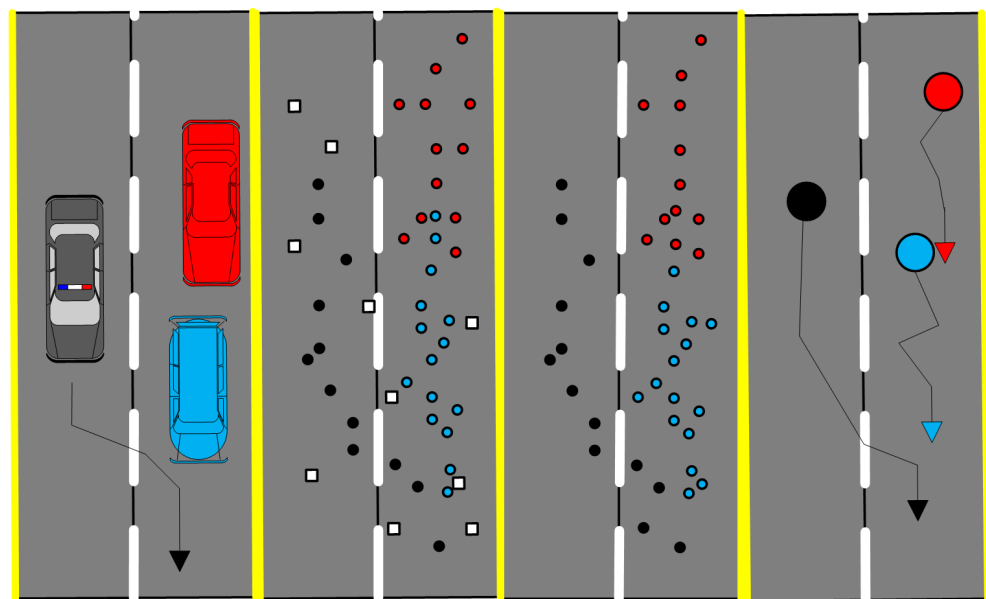


Figure 8. Schematic result of JPDA algorithm processing.

To evaluate the efficacy of the ASTEKF algorithm, we selected data from two tracks for comparison. Images of two vehicle targets in motion are displayed in Figure 9. For filtering and tracking, we selected two cars: vehicle A, which changes lanes while traveling, and vehicle B, which travels straight ahead. For around 11 seconds, from frame 90 to frame 305, vehicle A was tracked. For around nine seconds, from frame 81 to frame 260, vehicle B was tracked.

The tracking outcomes of the ASTEKF algorithm are shown in Figure 10. Analysis of the measurement data, filtered tracking data, and recorded video shows that the system is able to track the experimental vehicles steadily. Furthermore, following post-filtering, the tracking trajectory of the vehicle becomes more consistent, with small variances even in the case of measurement data points that are outliers. The target car's filtered trajectory matches the real motion state of the vehicle as it changes lanes, and the velocity filtering values converge without diverging. As shown in Figure 11 and Table 4, the error in radial velocity is less than 0.3 m/s and the accurate measurement point velocity values is less than 0.1 m/s once the ASTEKF algorithm has converged.

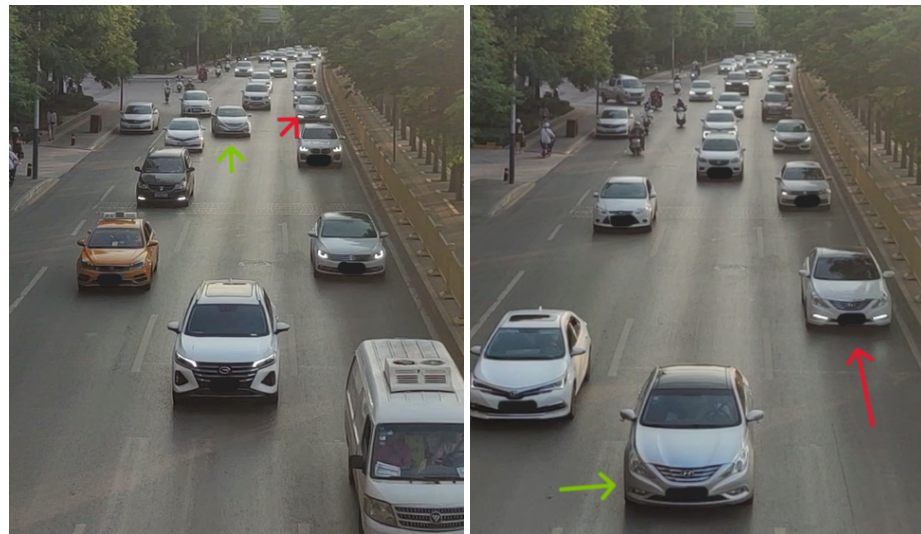


Figure 9. Vehicle target pictures.

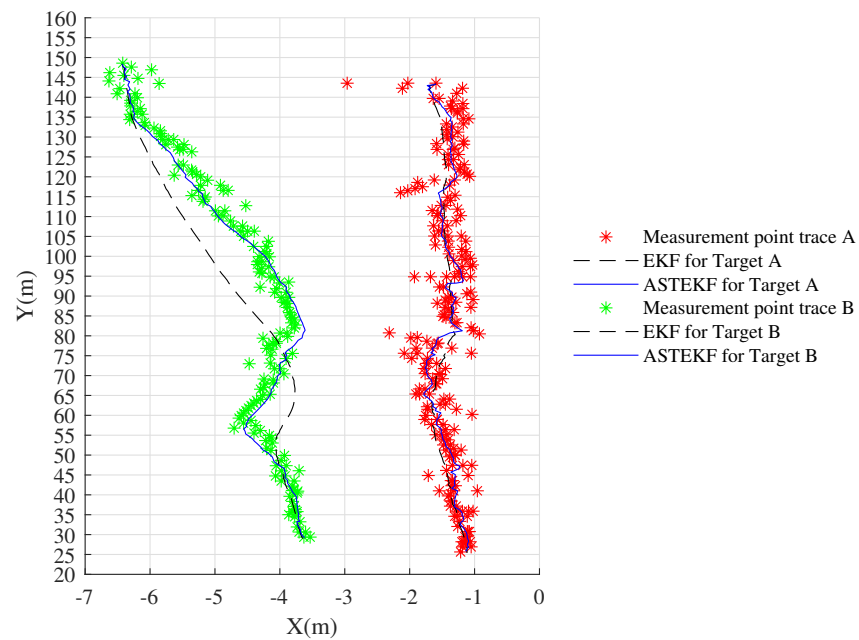


Figure 10. Result of ASTEKF tracking.

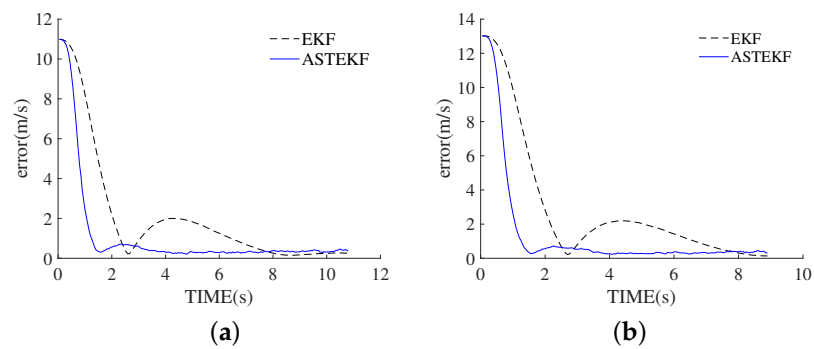
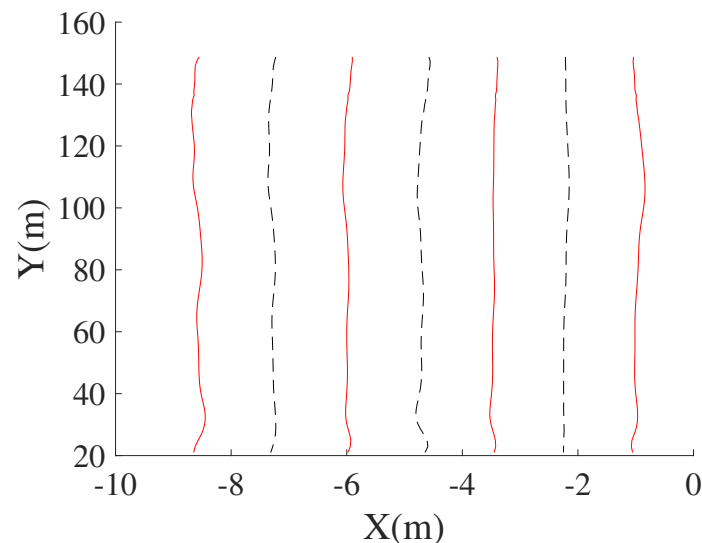


Figure 11. Tracking results of radial velocity error. (a) Tracking error for target A. (b) Tracking error for target B.

Table 4. Mean error table.

Algorithms	A X-Axis (m/s)	A Y-Axis (m/s)	B X-Axis (m/s)	B Y-Axis (m/s)
EKF	0.4332	1.7487	0.2328	1.4424
ASTEKF	0.2864	1.1259	0.1654	0.9534

As shown in Figure 12, using only radar data, the vehicle track is acquired following data processing, and the track information is then processed to obtain the main road lane. As a result, it is possible to carry out lane change judgment, traffic flow statistics, and other applications.

**Figure 12.** Division results of main vehicle routes.

The empirical results indicate that the ASTEKF algorithm meets realistic traffic application requirements and exhibits favorable estimation performance in real-world traffic settings.

4. Conclusions

The ASTEKF algorithm, which can handle environmental interference and navigate urban streets, is proposed in this paper as a potential solution to the tracking vehicle targets problem. ASTEKF improves the Extended Kalman Filter's capability by utilizing strong tracking theory to increase state estimate accuracy and real-time capabilities. Secondly, by using a least squares method for covariance update computations, several suboptimal fading factors and locally optimal weak factors are used, improving adaptive adjustment capability and providing a workable suggestion for enhancing the millimeter-wave monitoring radar's filtering algorithm.

Author Contributions: Conceptualization, F.T.; methodology, W.F.; software, W.F. and X.G.; validation, X.G., F.T. and W.F.; investigation, F.T.; data curation, W.F.; writing—original draft preparation, X.G.; writing—review and editing, F.T.; Supervision, F.T. All authors have read and agreed to the published version of the manuscript.

Funding: This research was funded by the Shaanxi Provincial Science and Technology Plan Project (No. 2020GY-029).

Data Availability Statement: Data are contained within the article.

Conflicts of Interest: The authors declare no conflicts of interest.

References

1. Guerrero-Ibáñez, J.; Zeadally, S.; Contreras-Castillo, J. Sensor technologies for intelligent transportation systems. *Sensors* **2018**, *18*, 1212. [[CrossRef](#)]
2. Wang, K.; Xiong, H.; Zhang, J.; Chen, H.; Dou, D.; Xu, C.-Z. SenseMag: Enabling Low-Cost Traffic Monitoring Using Noninvasive Magnetic Sensing. *IEEE Internet Things J.* **2021**, *8*, 16666–16679. [[CrossRef](#)]
3. Zhu, B.; Sun, Y.; Zhao, J.; Zhang, S.; Zhang, P.; Song, D. Millimeter-Wave Radar in-the-Loop Testing for Intelligent Vehicles. *IEEE Trans. Intell. Transp. Syst.* **2021**, *23*, 11126–11136. [[CrossRef](#)]
4. Zhao, C.; Ding, D.; Du, Z.; Shi, Y.; Su, G.; Yu, S. Analysis of perception accuracy of roadside millimeter-wave radar for traffic risk assessment and early warning systems. *Int. J. Environ. Res. Public Health* **2023**, *20*, 879. [[CrossRef](#)] [[PubMed](#)]
5. Zhang, T.; Jin, P.J. Roadside lidar vehicle detection and tracking using range and intensity background subtraction. *J. Adv. Transp.* **2022**, *2022*, 2771085. [[CrossRef](#)]
6. Wang, G.; Wu, J.; Xu, T.; Tian, B. 3D vehicle detection with RSU LiDAR for autonomous mine. *IEEE Trans. Veh. Technol.* **2021**, *70*, 344–355. [[CrossRef](#)]
7. Deshmukh, P.; Satyanarayana, G.; Majhi, S.; Sahoo, U.K.; Das, S.K. Swin transformer based vehicle detection in undisciplined traffic environment. *Expert Syst. Appl.* **2023**, *213*, 118992. [[CrossRef](#)]
8. Othmani, M. A vehicle detection and tracking method for traffic video based on faster R-CNN. *IEEE Internet Things J.* **2022**, *81*, 28347–28365. [[CrossRef](#)]
9. Qiu, Y.; Lu, Y.; Wang, Y.; Jiang, H. IDOD-YOLOV7: Image-Dehazing YOLOV7 for Object Detection in Low-Light Foggy Traffic Environments. *Sensors* **2023**, *23*, 1347. [[CrossRef](#)] [[PubMed](#)]
10. Jafari-Sadeghi, V.; Garcia-Perez, A.; Candelero, E.; Couturier, J. Exploring the impact of digital transformation on technology entrepreneurship and technological market expansion: The role of technology readiness, exploration and exploitation. *J. Bus. Res.* **2021**, *124*, 100–111. [[CrossRef](#)]
11. Shi, J.; Tang, Y.; Gao, J.; Piao, C.; Wang, Z. Multitarget-tracking method based on the fusion of millimeter-wave radar and LiDAR sensor information for autonomous vehicles. *Sensors* **2023**, *23*, 6920. [[CrossRef](#)]
12. Shahian Jahromi, B.; Tulabandhula, T.; Cetin, S. Real-time hybrid multi-sensor fusion framework for perception in autonomous vehicles. *Sensors* **2019**, *19*, 4357. [[CrossRef](#)]
13. Sun, C.; Li, Y.; Li, H.; Xu, E.; Li, Y.; Li, W. Forward Collision Warning Strategy Based on Millimeter-Wave Radar and Visual Fusion. *Sensors* **2023**, *23*, 9295. [[CrossRef](#)] [[PubMed](#)]
14. Zhang, L.; Mao, D.; Niu, J.; Wu, Q.J.; Ji, Y. Continuous tracking of targets for stereoscopic HFSWR based on IMM filtering combined with ELM. *Remote Sens.* **2022**, *12*, 272. [[CrossRef](#)]
15. Liu, Z.; Chen, Y.; Lu, Y. Mid-state Kalman filter for nonlinear problems. *Sensors* **2022**, *22*, 1302. [[CrossRef](#)] [[PubMed](#)]
16. Emami, A.; Sarvi, M.; Asadi Bagloee, S. Using Kalman filter algorithm for short-term traffic flow prediction in a connected vehicle environment. *J. Mod. Transp.* **2019**, *27*, 222–232. [[CrossRef](#)]
17. An, Q.; Cai, Y.; Zhu, J.; Wang, S.; Han, F. Multi-Target Tracking Algorithm Combined with High-Precision Map. *Sensors* **2022**, *22*, 9371. [[CrossRef](#)] [[PubMed](#)]
18. Kalman, R.E. A new approach to linear filtering and prediction problems. *J. Basic Eng.* **1960**, *82*, 35–45. [[CrossRef](#)]
19. Gong, B. Kalman Filter-based Signal Processing for Robot Target Tracking. *Int. J. Adv. Comput. Sci. Appl.* **2023**, *14*, 589–597. [[CrossRef](#)]
20. Cai, L.; Zhang, Z.; Yang, J.; Yu, Y.; Zhou, T.; Qin, J. A noise-immune Kalman filter for short-term traffic flow forecasting. *Phys. A Stat. Mech. Its Appl.* **2019**, *536*, 122601. [[CrossRef](#)]
21. Khalkhali, M.B.; Vahedian, A.; Yazdi, H.S. Situation assessment-augmented interactive Kalman filter for multi-vehicle tracking. *IEEE Trans. Intell. Transp. Syst.* **2021**, *23*, 3766–3776. [[CrossRef](#)]
22. Ye, X.; Wang, J.; Wu, D.; Zhang, Y.; Li, B. A Novel Adaptive Robust Cubature Kalman Filter for Maneuvering Target Tracking with Model Uncertainty and Abnormal Measurement Noises. *J. Abbr.* **2023**, *23*, 6966. [[CrossRef](#)]
23. Pang, H.; Wang, P.; Wang, M.; Hu, C. On accurate estimation of vehicle lateral states based on an improved adaptive unscented Kalman filter. *Proc. Inst. Mech. Eng. Part D J. Automob. Eng.* **2022**, 09544070221132328. [[CrossRef](#)]
24. Chen, N.; Zhao, L.; Lou, T.-S.; Li, C. Adaptive fast desensitized ensemble Kalman filter for uncertain systems. *Signal Process.* **2023**, *202*, 108767. [[CrossRef](#)]
25. Ge, Q.; Hu, X.; Li, Y.; He, H.; Song, Z. A Novel Adaptive Kalman Filter Based on Credibility Measure. *IEEE/CAA J. Autom. Sin.* **2023**, *10*, 103–120. [[CrossRef](#)]
26. Kalman, R.E.; Bucy, R.S. New results in linear filtering and prediction theory. *J. Basic Eng.* **1961**, *83*, 95–108. [[CrossRef](#)]
27. Na, W.; Yoo, C. Real-Time Parameter Estimation of a Dual-Pol Radar Rain Rate Estimator Using the Extended Kalman Filter. *Remote Sens.* **2021**, *13*, 2365. [[CrossRef](#)]
28. Wei, L.; Chen, J.; Ding, Y.; Wang, F.; Zhou, J. Adaptive tracking of high-maneuvering targets based on multi-feature fusion trajectory clustering: LPI's purpose. *Sensors* **2022**, *22*, 4713. [[CrossRef](#)]
29. Qiao, S.; Fan, Y.; Wang, G.; Mu, D.; He, Z. Radar Target Tracking for Unmanned Surface Vehicle Based on Square Root Sage–Husa Adaptive Robust Kalman Filter. *Sensors* **2022**, *22*, 2924. [[CrossRef](#)] [[PubMed](#)]
30. Kaniewski, P.; Kraszewski, T. Estimation of Handheld Ground-Penetrating Radar Antenna Position with Pendulum-Model-Based Extended Kalman Filter. *Remote Sens.* **2023**, *15*, 741. [[CrossRef](#)]

31. Zerdali, E.; Yildiz, R.; Inan, R.; Demir, R.; Barut, M. Improved speed and load torque estimations with adaptive fading extended Kalman filter. *Int. Trans. Electr. Energy Syst.* **2021**, *31*, e12684. [[CrossRef](#)]
32. Zhang, X.; Pei, W.; Yin, X.; Yuan, S. An observation algorithm for key motion states of skid-steered wheeled unmanned vehicle. *Proc. Inst. Mech. Eng. Part D J. Automob. Eng.* **2023**, *237*, 2431–2443. [[CrossRef](#)]
33. Liu, J.; Wang, P.; Zha, F.; Guo, W.; Jiang, Z.; Sun, L. A strong tracking mixed-degree cubature kalman filter method and its application in a quadruped robot. *Sensors* **2020**, *20*, 2511. [[CrossRef](#)] [[PubMed](#)]
34. Zhang, Y.; Zhang, S.; Gao, Y.; Li, S.; Jia, Y.; Li, M. Adaptive square-root unscented kalman filter phase unwrapping with modified phase gradient estimation. *Remote Sens.* **2022**, *14*, 1229. [[CrossRef](#)]
35. Ge, Q.; Shao, T.; Chen, S.; Wen, C. Carrier tracking estimation analysis by using the extended strong tracking filtering. *IEEE Trans. Ind. Electron.* **2017**, *64*, 1415–1424. [[CrossRef](#)]
36. Zhang, A.; Shuida, B.; Fei, G.; Wenhao, B. A novel strong tracking cubature Kalman filter and its application in maneuvering target tracking. *Chin. J. Aeronaut.* **2019**, *32*, 2489–2502. [[CrossRef](#)]
37. Ge, Z.; Jia, G.; Zhi, Y.; Zhang, X.; Zhang, J. Strong tracking extended particle filter for manoeuvring target tracking. *IET Radar Sonar Navig.* **2020**, *14*, 1708–1716. [[CrossRef](#)]
38. Zhang, Y.; Li, M.; Zhang, Y.; Hu, Z.; Sun, Q.; Lu, B. An enhanced adaptive unscented kalman filter for vehicle state estimation. *IEEE Trans. Instrum. Meas.* **2022**, *71*, 1–12. [[CrossRef](#)]
39. Takyi-Aninakwa, P.; Wang, S.; Zhang, H.; Li, H.; Yang, X.; Fernandez, C. An ASTSEKF optimizer with nonlinear condition adaptability for accurate SOC estimation of lithium-ion batteries. *J. Energy Storage* **2023**, *70*, 108098. [[CrossRef](#)]
40. Zhou, D.; Xi, Y.G.; Zhang, Z. A suboptimal multiple fading extended Kalman filter. *Acta Autom. Sin.* **1991**, *17*, 689–695. Available online: <http://www.aas.net.cn/article/id/14540> (accessed on 13 May 2023).
41. Yang, B.; Zhang, H.; Chen, Y.; Zhou, Y.; Peng, Y. Urban Traffic Imaging Using Millimeter-Wave Radar. *Remote Sens.* **2022**, *14*, 5416. [[CrossRef](#)]
42. Kumuda, D.; Vandana, G.; Pardhasaradhi, B.; Raghavendra, B.; Srihari, P.; Cenkeramaddi, L.R. Multitarget Detection and Tracking by Mitigating Spot Jammer Attack in 77-GHz mm-Wave Radars: An Experimental Evaluation. *IEEE Sens. J.* **2022**, *23*, 5345–5361. [[CrossRef](#)]
43. Zhang, Z.; Wang, X.; Huang, D.; Fang, X.; Zhou, M.; Mi, B. iDT: An Integration of Detection and Tracking toward Low-Observable Multipedestrian for Urban Autonomous Driving. *IEEE Trans. Ind. Inform.* **2023**, *19*, 9887–9897. [[CrossRef](#)]
44. Bai, J.; Li, S.; Huang, L.; Chen, H. Robust detection and tracking method for moving object based on radar and camera data fusion. *IEEE Sens. J.* **2021**, *21*, 10761–10774. [[CrossRef](#)]

Disclaimer/Publisher’s Note: The statements, opinions and data contained in all publications are solely those of the individual author(s) and contributor(s) and not of MDPI and/or the editor(s). MDPI and/or the editor(s) disclaim responsibility for any injury to people or property resulting from any ideas, methods, instructions or products referred to in the content.